Received: 30 January 2024 | Revised: 20 August 2024 | Accepted: 19 September 2024

DOI: 10.1002/inc2.12027

WILEY

RESEARCH ARTICLE

Numerical simulation of electrically pumped active vertical-cavity surface-emitting lasers diodes based on metal halide perovskite

Renjun Liu[1] | **Hong Ji**[1] | **Diyar Mousa Othman**[1] | **Alexander R. C. Osypiw**[1] | **William Solari**[1] | **Wenlong Ming**[2] | **Jung Inn Sohn**[3] | **Jae Cheol Shin**[4] | **Bo Hou**[1]

[1]School of Physics and Astronomy, Cardiff University, Cardiff, UK

[2]School of Engineering, Cardiff University, Cardiff, UK

[3]Division of Physics and Semiconductor Science, Dongguk University-Seoul, Seoul, Republic of Korea

[4]Division of Electronics and Electrical Engineering, Dongguk University-Seoul, Seoul, Republic of Korea

Correspondence
Jung Inn Sohn, Jae Cheol Shin and Bo Hou.
Email: junginn.sohn@dongguk.edu, jcshin@dgu.ac.kr and Houb6@cardiff.ac.uk

Funding information
EPSRC SWIMS, Grant/Award Number: EP/V039717/1; Royal Society, Grant/Award Numbers: IEC\NSFC\211201, RGS\R1\221009; Leverhulme Trust, Grant/Award Number: RPG-2022-263; Sêr Cymru program – Enhancing Competitiveness Equipment Awards 2022-23, Grant/Award Number: MA/VG/2715/22-PN66

Abstract

Metal halide perovskites (MHP)-based electrically pumped vertical-cavity surface-emitting lasers (EPVCSEL) are promising candidates in optoelectronics due to low-carbon footprint solution processing method. However, significant challenges impede MHP-EPVCSEL manufacturing: (1) Distributed Bragg Reflectors (DBRs) composed of typical electron transport layers (ETLs) and hole transport layers (HTLs) are not conductive enough. (2) Due to large mobility difference of typical ETLs and HTLs, carriers-unbalanced injection leads to severe performance degradation. Herein, we propose a potential strategy to address such challenges using $MAPbCl_3$ and $CsSnCl_3$ as carrier transport layers with mobility 3 orders larger than typical ETLs and HTLs. Via transfer matrix method calculations, we find that the reflectance of DBRs composed of $MAPbCl_3$ (130.5 nm)/$CsSnCl_3$ (108 nm) is larger than 91% with 10 pairs of DBRs. Furthermore, the proposed EPVCSEL device simulation shows that MHP-EPVCSEL has the potential to achieve room temperature continuous wave lasing with a threshold current density of ~69 A cm^{-2} and output optical power ~10^{-4} W. This work can provide a deep insight into the practical realization of MHP-EPVCSEL.

KEYWORDS
laser, $MAPbCl_3$ and $CsSnCl_3$, perovskite, VCSEL

1 | INTRODUCTION

Vertical-cavity surface-emitting lasers (VCSEL) have a structure of a gain material sandwiched between a top mirror and bottom mirror with high reflectivity. Especially, when VCSEL is electrically pumped, the light emitting direction is vertical to the cavity surface. The property of electrically pumped vertical-cavity surface-emitting lasers (EPVCSEL) is of great significance and has been widely used in various fields, including fiber

optic communications,[1] laser printers,[2] and high-density data interconnects in computer chips.[3] Significantly, owing to features such as miniaturization, closely packed structure, and easy integration, EPVCSEL arrays integrated on one chip can be used to achieve high output power (larger than 100 W). However, the commonly used fabrication techniques in III-V semiconductors are complicated vacuum epitaxial deposition processes such as metal-organic chemical vapor deposition, which is undesirable for future Net Zero smart manufacturing.[4–6]

Solution-processed metal halide perovskite (MHP) materials have been rapidly progressed in photovoltaic devices and light-emitting diodes.[7] The corresponding device fabrication techniques have been fully developed, mainly based on low-carbon footprint approaches such as spin coating,[8,9] doctor blading,[10] and ink printing.[11] Based on these methods, perovskite-based solar cells have obtained power conversion efficiency beyond 25%[12] and the external quantum efficiency of perovskite-based light-emitting diodes (PeLEDs) is larger than 20%.[13–15] Recently, research on MHP-based VCSEL devices has been emerging, which have successfully demonstrated optically pumped VCSEL (OPVCSEL) devices with lasing wavelength covering from green to red spectrum.[16] However, as far as we know, there is no report on MHP-based EPVCSEL (MHP-EPVCSEL) and numerical modellings of the device have also not been constructed so far for which several difficulties should be taken into account. Firstly, the materials of the optical resonant cavity (such as Distributed Bragg Reflector-DBR) need to be electrically well conductive as well as highly reflective optically, allowing for fast injection of carriers and net optical gain. Secondly, the band structure and conductivity of DBRs need to be simultaneously matched in the device, allowing for balanced carrier injection. However, the difficulties cannot be overcome by typical electron transport layer (ETL) and hole transport layer (HTL) owing to the relatively low conductivity as well as the difference in electron and hole mobility. For example, ZnO as the typical ETL has a refractive index (n_{ref}) of 1.7 at 950 nm[17] and Poly(9,9-dioctylfluorene-alt-N-(4-sec-butylphenyl)-diphenylamine) (TFB) has an n_{ref} of 1.6 at 950 nm.[18] In this work, the designed lasing wavelength (λ) is 950 nm. If n_{ref} is set to about 2, 40 pairs of DRB (including top DBR and bottom DBR) are needed to achieve high reflectivity (99%) and the total thickness of DBRs account for 9.5 μm as the thickness (t) of each layer in DBRs should satisfy the relationship of $t = \lambda/(4n_{ref})$, which is over 95 times thicker than a typical PeLED and CdSe-based (thickness ~100 nm) excluding the thickness of electrodes.[19,20] It is obvious that the typical ETL and HTL materials in PeLED structure cannot be used as DBRs due to the poor electron and hole mobility (of the order of 10^{-6}-10^{-3} $cm^2V^{-1}s^{-1}$), which can lead to a large series resistance and generate heat and unbalanced carrier injection.[21,22] Therefore, optimal design of DBRs that are optically and electrically well fitted is the key to realize MHP-EPVCSEL. Besides, since the reports on numerical simulation of MHP-EPVCSEL are so limited, model-building on MHP-EPVCSEL is necessarily urgent.

Herein, we propose a comprehensive simulation study on using MHP materials as both cavity layer and active layer to realize an EPVCSEL. The MHP-EPVCSEL is designed based on a top-bottom structure: Anode/Hole Injection Layer (HIL)/Top-Distributed Bragg Reflector (T-DBR)/Optical Amplification Enhanced Layer1 (OAEL1)/ Hole Transport Layer (HTL)/Active Layer (AL)/ETL (ETL)/Optical Amplification Enhanced Layer1 (OAEL2)/Bottom-Distributed Bragg Reflector (B-DBR)/ Electron Injection Layer (EIL)/Cathode. We found that DBRs constructed by using MHP materials can achieve both high reflectivity and good conductivity. Moreover, numerical simulation via SILVACO TCAD showed that our proposed device can successfully achieve continuous wave lasing.

2 | DEVICE SIMULATION

2.1 | Methodology

Calculations and numerical simulations were performed based on transfer matrix method MATLAB codes as well as the SILVACO TCAD package. Figure 1 shows the detailed simulation flow chart of EPVCSEL diodes. The major material parameters used in device performance simulation are listed in Table 1. Basically, the VCSEL simulator is based on physic models to perform electrical, thermal, and optical simulation of VCSEL using accurate, robust, and reliable fully numerical methods.[34] The following parameters can be achieved via VCSEL simulator: (1) Reflectivity of a VCSEL cavity as a function of the incident light wavelength and the resonant frequency of the cold cavity. (2) By solving the Helmholtz equation in cylindrical coordinates, optical intensity of emitted dominant mode can be calculated. (3) Optical gain in active layer as a function of the photon energies, quasi-Fermi levels, temperature, and optical intensity distribution can be calculated. (4) Photon density of emitted dominant mode. (5) The light output power.

Single frequency EPVCSEL diodes (operating at single longitudinal mode and single transverse mode) are strongly desired in practical applications. The VCSEL simulator is powerful in the simulation of single frequency EPVCSEL devices, and the subsequent simulations are all based on this. The simulations are conducted

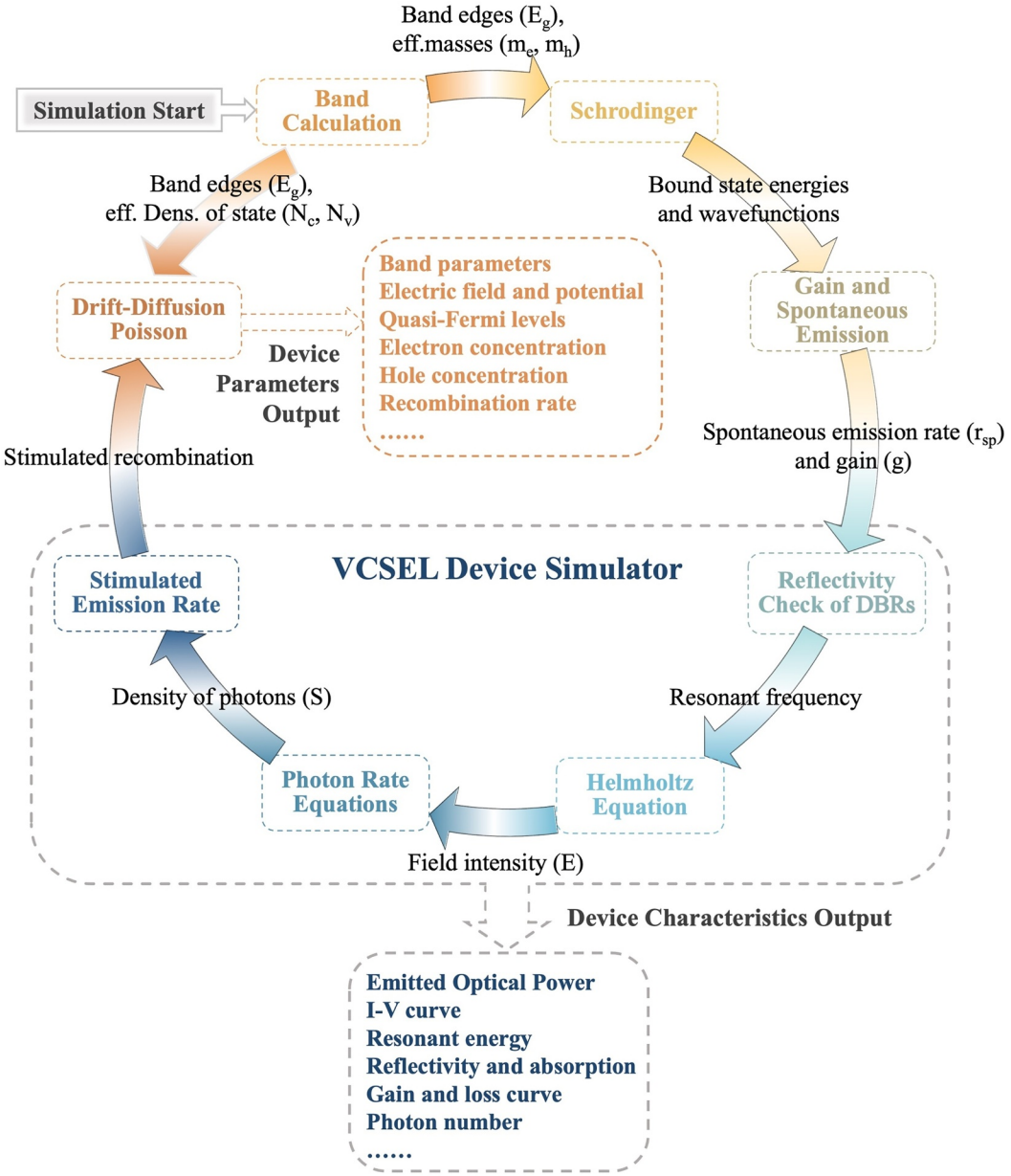

FIGURE 1 A flow chart of the VCSEL device simulation. VCSEL, vertical-cavity surface-emitting lasers.

in cylindrical coordinates, and the radius of the device is fixed at 6 μm. Electrically, the functions of MoO_3 and metallic cesium (Cs) are to form the Ohmic contacts to enhance the injection of carriers,[30] therefore, in the simulation, Ohmic contacts are directly specified using syntax. The simulations will focus on the optimizations of the doping concentration and thickness of HTL and ETL (i.e., OAEL1 and OAEL2). Subsequently, the optimized doping concentration and thickness are used to optimize the mobility. Later, the optimized parameters will be used to obtain the optimal value of the number of pairs (NP) of DBR. Finally, all the optimized parameters will be used in the simulation of the lattice heating effect of the device. The detailed optimization process can be found in supplementary information.

Typically, the simulation starts by inputting basic material parameters such as electron affinity, relative dielectric constant, carrier mobility, carrier lifetime, doping concentration, and thickness of material. Via band calculation, the bandgap and effective mass of carriers are obtained. These are used to calculate the bound state energies and corresponding wavefunctions of active layer via the Schrodinger solver. Later, the results are used to estimate gain and spontaneous emission rate by gain and spontaneous emission models. Then, the results are sent through the VCSEL simulator, which will first conduct cold cavity

TABLE 1 The main physical properties for various layers of the MHP-EPVCSEL device.

Symbol	Unit	Description	$CsSnCl_3$	$MAPbCl_3$	$CsSnI_3$
E_g	eV	Bandgap	2.9[23]	3.1[23]	1.3[23]
χ	eV	Electron affinity	3.5[23]	3.8[23]	4.3[23]
ε_r	-	Relative dielectric constant at 950 nm	4.84[24]	3.31[25]	5.75[26]
N_C	cm^{-3}	Effective density of state of conduction band	1×10^{19} [27]	1×10^{19}	1×10^{19} [27]
N_V	cm^{-3}	Effective density of state of valence band	1×10^{19} [27]	1×10^{19}	1×10^{18} [27]
m_e	-	Electron effective mass	~0.14[28]	~0.2[28]	~0.19[26]
m_h	-	Hole effective mass	~0.14[28]	~0.2[28]	~0.09[26]
μ_e	$cm^2V^{-1}s^{-1}$	Electron mobility	2~50[21,29]	2~50[29,30]	50[26]
μ_h	$cm^2V^{-1}s^{-1}$	Hole mobility	2~50[16,31]	2~50[29,30]	200[26]
τ_e	ns	Electron lifetime	1~10	1~10	1~10[26]
τ_h	ns	Hole lifetime	1~10	1~10	1~10[26]
N_D	cm^{-3}	Donor concentration	~10^{17}	~10^{17}	~10^{17} [32]
N_A	cm^{-3}	Acceptor concentration	~10^{17}	~10^{17}	~10^{17} [32]
κ	$Wcm^{-1}K^{-1}$	Thermal conductivity	~0.50[33]	~0.51[33]	~0.57[33]
C_V	$Jcm^{-3}K^{-1}$	Heat capacitance per unit volume	~1.12[33]	~1.62[33]	~1.3[33]

Abbreviations: EPVCSEL, electrically pumped vertical-cavity surface-emitting lasers; MHP, metal halide perovskites.

reflectivity experiments to confirm that the reflectivity is larger than 99% and determine the resonant frequency of the cold cavity. After that, the results are used to calculate the optical field intensity by the Helmholtz equation solver. Next, the gain and spontaneous emission rate together with the optical field intensity are used to calculate the photon number by solving photon rate equations. Subsequently, the results are used to calculate the stimulated recombination rate, which can be coupled into Poisson's equation and drift-diffusion model to obtain parameters such as electric potential and electric field distribution, quasi-fermi levels, carrier current etc. From the VCSEL simulator, device characteristics such as the I-V curve and P-V curve can be obtained.

2.2 | Device structure of MHP-EPVCSEL

The detailed structure of the as-proposed MHP-EPVCSEL device, from top to bottom is ITO-Anode (100 nm)/MoO_3-HIL (7 nm)/$CsSnCl_3$ (108 nm per layer)-$MAPbCl_3$ (130.5 nm per layer) –T-DBR (22 pairs)/$CsSnCl_3$-OAEL1 (188 nm)/HTL (130 nm)/$CsSnI_3$-AL (25 nm)/ETL (90 nm)/$CsSnCl_3$-OAEL2 (208 nm)/$CsSnCl_3$ (108 nm per layer)-$MAPbCl_3$ (130.5 nm per layer) –B-DBR (22 pairs)/Cs-EIL (0.5 nm)/Al-Cathode (100 nm)/Heat Sink as shown in Figure 2A. The energy band diagram of the corresponding device is shown in Figure 2B. Subsequently, the device performance simulations and optimizations were conducted based on Figure 2A. The proposed device fabrication process is detailed in supplementary information.

2.3 | The materials for DBRs

The MHP can meet the requirements of DBRs with micrometers thickness as well as good conductivities for both electron and hole. It is reported that the electron mobility of $MAPbCl_3$ is of the order of 0.9, 1.1 and 1.3 $cm^2V^{-1}s^{-1}$ for the thickness of 1, 2, and 3 μm,[30] respectively. In addition, the hole mobility of $MAPbCl_3$ was on the order of 2.1, 2.5 and 2.9 $cm^2V^{-1}s^{-1}$ for the thickness of 1, 2, and 3 μm,[30] respectively. Thus, the hole mobility and electron mobility of $MAPbCl_3$ are 3 orders higher than that of commonly used ETL (ZnO nanoparticles~10^{-3} $cm^2V^{-1}s^{-1}$ [21]) and HTL (TAPC~10^{-3} $cm^2V^{-1}s^{-1}$ [24]). Therefore, the $MAPbCl_3$ has a well-balanced hole and electron mobility and can be used for transferring both hole and electron, and more importantly, the mobility for carriers tends to be higher with the increase of thickness. In addition, the performance of a device with 50 nm $MAPbCl_3$ being used as both ETL and HTL is comparable to that of a device with 1000 nm $MAPbCl_3$ for both ETL and HTL. This implies that the electron mobility and hole mobility at 50 nm $MAPbCl_3$ are comparable with that of $MAPbCl_3$ at 1000 nm. Similar results have also been found for $CsSnCl_3$.[30] Therefore, $CsSnCl_3$ and $MAPbCl_3$ will be employed as both DBRs and

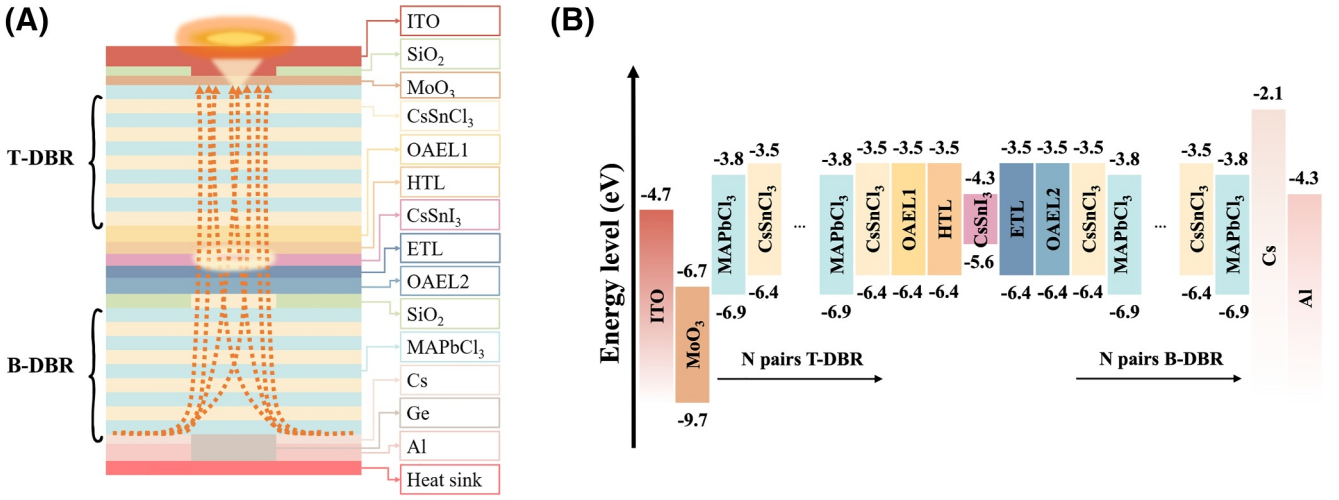

FIGURE 2 (A) The proposed schematic structure of the MHP-EPVCSEL device and (B) the electronic energy band diagram of the corresponding device. EPVCSEL, electrically pumped vertical-cavity surface-emitting lasers.

charge transport layers in the following MHP-EPVCSEL simulations.

2.4 | The material for the active layer

$CsSnI_3$ is chosen as a gain material due to heavy metal-free inorganic nature, excellent electrical and optical properties.[32] Electrically, it's a p-type semiconductor with high mobility (~585 $cm^2V^{-1}s^{-1}$) comparable with that of InP (~700 $cm^2V^{-1}s^{-1}$).[32] Optically, it has a bandgap of 1.3 eV, comparable with InP with the bandgap of 1.3 eV, and shows strong near-infrared (NIR) photoluminescence (PL) intensity at 950 nm when excited with a 533 nm laser, and the PL intensity of $CsSnI_3$ is several times larger than that of InP wafer.[32] Besides, $CsSnI_3$ based NIR LEDs have already been successfully fabricated with high quantum efficiency.[35] Therefore, solution-processed $CsSnI_3$ is a promising alternative employed as active layer in MHP-EPVCSEL device.

2.5 | The materials for EIL, HIL, and ETL, HTL and OAEL1, OAEL2

Metallic Cs and MoO_3 (n_{ref}~2.1 at 950 nm[31]) were used as EIL and HIL, respectively, to form ohmic contacts and improving carriers' injection. Germanium (Ge) is used to enhance the reflectance of B-DBR due to its large refractive index (n_{ref}~4.5 at 950 nm) and extremely low extinction coefficient.[36] As mentioned above, $MAPbCl_3$ and $CsSnCl_3$ have high mobility and can both transfer hole and electron simultaneously; therefore, we use $CsSnCl_3$ as both ETL and HTL layers in our simulation. The function of OAEL1 and OAEL2 is to adjust the cavity length, thus tuning the wavelength of the emitted longitudinal mode. Also, the OAEL1 and OAEL2 need to be hole and electron conductive. Therefore, $CsSnCl_3$ is also used as OAEL1 and OAEL2 from band alignment prospects, as shown in Figure 2B.

3 | RESULTS AND DISCUSSION

3.1 | The estimation of reflectance of DBRs using matrix transfer method

Figure 3 shows the simulation results to demonstrate the feasibility of the as-proposed MHP-EPVCSEL under the bottom DBR (B-DBR) and top DBR (T-DBR) device configurations calculated using the matrix transfer method.[37] In this simulation, when the light incidence angle is perpendicular to the material, we can obtain the results of reflectance of B-DBR and T-DBT with the NP corresponding to 22, 15, 10, 8, and 5, respectively. When N_P is greater than 10, both B-DBR and T-DBR present reflectance larger than 91%, which satisfies the requirements of good reflectors.[38] When N_P is equal to 22, the reflectance of both DBRs is larger than 99%, and the reflectance of B-DBR is slightly higher; therefore, the longitudinal mode lasing with the wavelength of 950 nm will be realized from the top. Detailed parameters and simulation results for reflectance are shown in Table 2. It is worth noting that the reflectivity of the cold cavity must be larger than 99%, which is required by the VCSEL simulator in Silvaco-TCAD. These reflectance results will be fed to the numerical simulation of the MHP-EPVCSEL device by the VCSEL simulator.

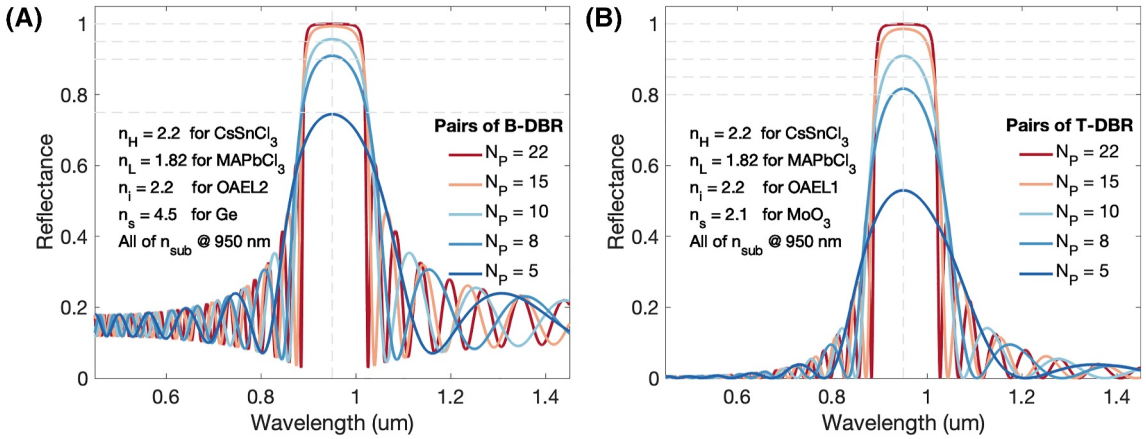

FIGURE 3 The reflectance of (A) Bottom DBRs and (B) top DBRs with the pairs of DBR of 5, 8, 10, 15 and 22, respectively. n_{sub} refers to the refractive index of corresponding material. NP refers to the NP of DBRs. In B-DBR and T-DBR, n_H refers to high refractivity material, n_L refers to low refractivity material, n_i refers to the material which light enters in, and n_s refers to the material which light comes out. DBRs, Distributed Bragg Reflectors; NP, Number of pairs.

TABLE 2 The parameters of DBRs simulated by TMM.

Parameters	Bottom-DBR (B-DBR)	Top-DBR (T-DBR)
n_H	2.2	2.2
n_L	1.82	1.82
n_i	2.2	2.2
n_s	4.5	2.1
Incidence angle (degree)	0	0
Bragg wavelength (nm)	950	950
$N_P = 22$	99.95%	99.9%
$N_P = 15$	99.3%	98.6%
$N_P = 10$	95.7%	91%
$N_P = 8$	91%	81.7%
$N_P = 5$	74.5%	53%

Abbreviations: DBRs, Distributed Bragg Reflectors; TMM, transfer matrix method.

3.2 | The effects of mobility on device performance

Carriers' mobility is an important material parameter that affects device performance since HTL, ETL, OAEL1, OAEL2, T-DBR, B-DBR and active layer all involve halide perovskites which are $MAPbCl_3$, $CsSnCl_3$ and $CsSnI_3$. The mobilities of $MAPbCl_3$ and $CsSnCl_3$ need to be comparable with each other.[30] Depending on the crystallinity, the mobility of $MAPbCl_3$ ranges from 2 to 51 $cm^2V^{-1}s^{-1}$,[29,30] and for $CsSnI_3$, the value of mobility can reach several hundred.[32] Therefore, in this simulation we use an average value of mobility (μ) to represent the electron and hole mobility of each layer. The selected μ ranges from 2 to 100 $cm^2V^{-1}s^{-1}$.

As shown in Figure 4A, the output power P_{out} is proportional to the injection current after the injection current passes the threshold at a certain mobility. This is consistent with the theoretical prediction since $P_{out} = \eta_{exe} \cdot (i/e) \cdot h\gamma$.[39] Therefore, the injection current increases with the increase of mobility leading to the increase of P_{out}. Besides, the threshold decreases with the increase of mobility. The mobility has no effect on reflectivity, absorption loss and resonant photon energy, as can be seen from Figure 4B–C. Since the absorption is related to the thickness of the emitting layer, which is 25 nm, the absorption loss is small, and can be treated as constant with the change in mobility, the maximum gain is almost unchanged at different mobility, as shown in Figure 5B. The gain is closely related to the difference in quasi-Fermi levels of electron and hole

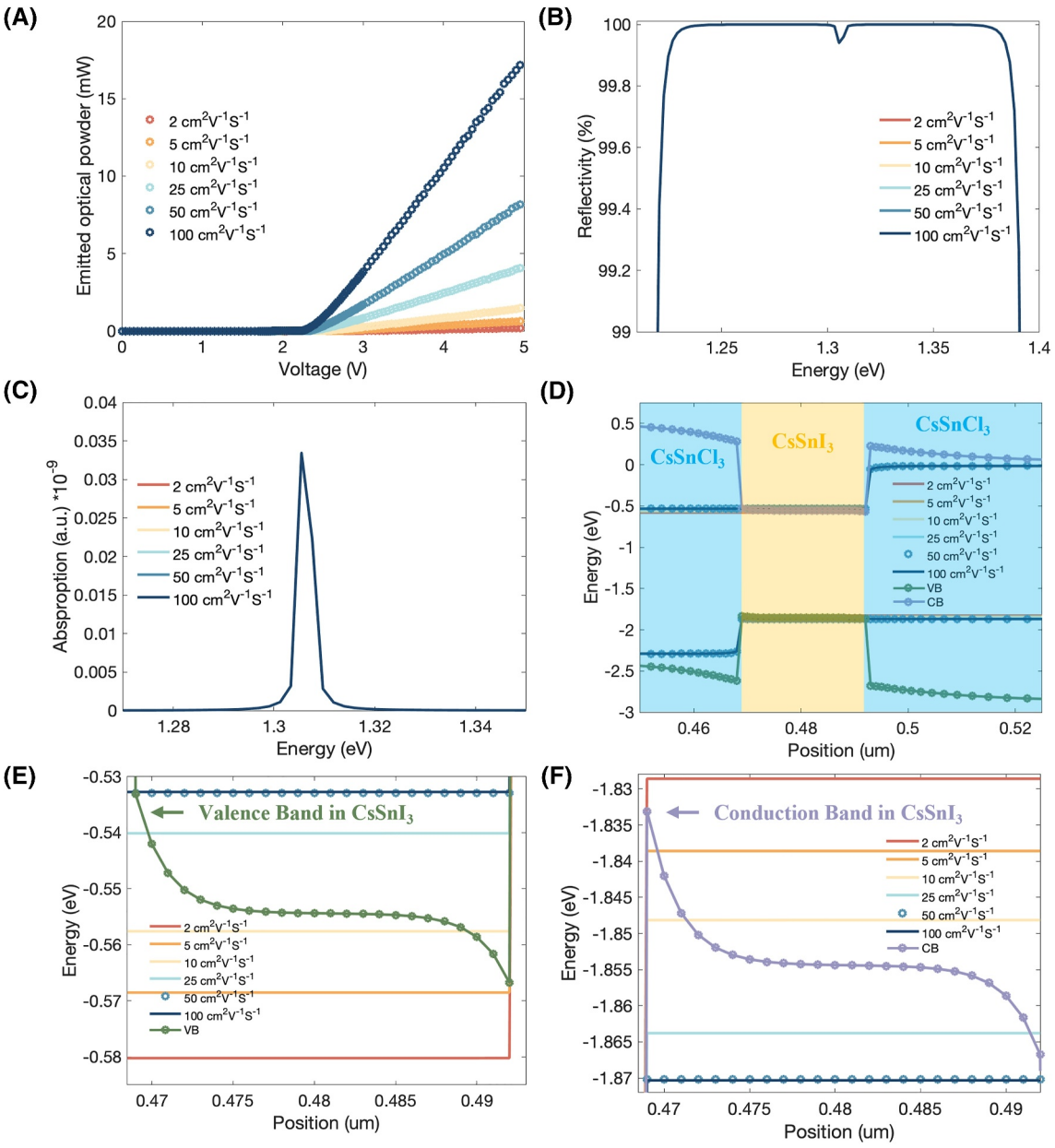

FIGURE 4 At different mobility values ranging from 2 to 100 $cm^2V^{-1}s^{-1}$, (A) the P-V curve, (B) the reflectivity spectrum of Distributed Bragg Reflector (DBR), (C) the absorption spectrum of DBR, (D) the energy band diagram for the structure of $CsSnCl_3/CsSnI_3/CsSnCl_3$ with the applied voltage of 2.3 V, (E) the enlarged part of conduction band and quasi-Fermi levels of electron in active region, and (F) the enlarged valence band and quasi-Fermi levels of hole in active region. DBR, Distributed Bragg Reflector.

($\Delta E_{fnp} = E_{fn} - E_{fp}$), which are determined by injection current. The gain cannot keep increasing with injection current because the increase of injection current leads to the increase of ΔE_{fnp}, which will mainly enhance stimulated recombination; however, the enhanced stimulated recombination will in turn consume both electron and hole allowing more optical power to be generated and thus reducing ΔE_{fnp}. Therefore, with the increase of injection current, the gain profile rapidly increases to maximum value and then decreases to a stable value that is slightly larger than the loss allowing for the stimulated recombination and lasing, in which state the ΔE_{fnp} should be larger than bandgap of active layer material ($\Delta E_{fnp} > E_g$). If ΔE_{fnp} is smaller than E_g ($\Delta E_{fnp} < E_g$), this means that gain is smaller than loss, stimulated recombination cannot be triggered and, in this stage, the radiative recombination is dominated by the spontaneous recombination. The above process can be further illustrated from Figure 4D–F) from the perspective of the evolution of quasi-fermi levels of carriers. When $\mu \leq 5\ cm^2V^{-1}s^{-1}$, both E_{fn} and E_{fp} are not entering the conduction band (E_{CB}) and valence band (E_{VB}); therefore, $\Delta E_{fnp} < E_g$, the spontaneous

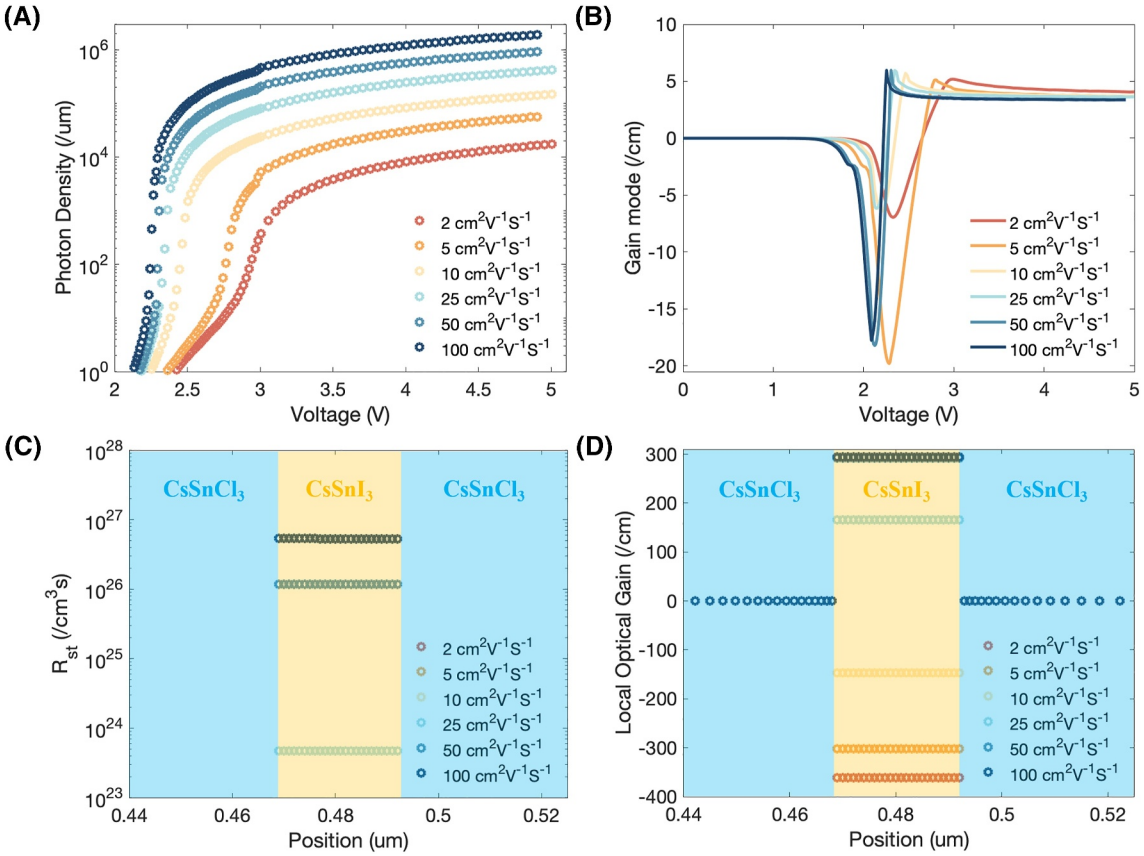

FIGURE 5 At different mobility values ranging from 2 to 100 $cm^2V^{-1}s^{-1}$, (A) the photon density and (B) the gain versus applied voltage, (C) the stimulated recombination rate in active layer ($CsSnI_3$) and electron transport region ($CsSnCl_3$) and (D) the local optical gain at active layer ($CsSnI_3$) and hole transport region ($CsSnCl_3$) with the applied voltage of 2.3 V.

recombination dominates. When μ increases to 10 $cm^2V^{-1}s^{-1}$, E_{fn} and E_{fp} are only partially entering into E_{CB} and E_{VB}, but the ΔE_{fnp} is still less than the effective E_g. Therefore, the spontaneous recombination still dominates but stimulated recombination begins to rise. Until now, the local optical gains at the active region are negative and a negative gain equates to a loss, and for the stimulated recombination rate (R_{st}), the values are rather small, as shown in Figure 5C,D). When μ further increases to 25 $cm^2V^{-1}s^{-1}$, E_{fn} and E_{fp} are almost totally entering into E_{CB} and E_{VB}, so ΔE_{fnp} is larger than the effective E_g and stimulated recombination becomes dominant. When μ increases from 50 to 100 $cm^2V^{-1}s^{-1}$, injection current still increases, but E_{fn} and E_{fp} almost stay the same and local optical gain tends to be saturated. This is because the stimulated recombination rate R_{st} increases at the cost of consuming electrons and holes generated by the increased injection current under large mobility, as shown in Figure 5C. Stimulated recombination can contribute to photon density, which is shown in Figure 5A.

Based on our simulation results, the device performance enhances with the increase in mobility. At this moment, the reported mobility of both electron and hole is in the order of 2 $cm^2V^{-1}s^{-1}$ for both $MAPbCl_3$ and $CsSnCl_3$ and it increases with thickness.[30] The reported value for $CsSnI_3$ is higher which can be up to an order of several hundred.[32] Since the mobility of electrons is comparable with that of holes for $MAPbCl_3$ and $CsSnCl_3$. Therefore, the mobility value of both electron and hole is set to 5 $cm^2V^{-1}s^{-1}$ is a reasonable and achievable value in practical devices.[40]

3.3 | The effects of DBR pairs on device performance

The NP of DBR layers is a significant parameter that influences the quality of the DBR optical resonant cavity.[41] In this simulation, N_P for both T-DBR and B-DBR increases from 19 to 25. As shown in Figure 6A, the threshold voltage decreases with the increase of N_P and this can be attributed to the absorption loss and reduced reflectivity, both of which decrease with the increase of N_P as shown in Figure 6B,D. This is

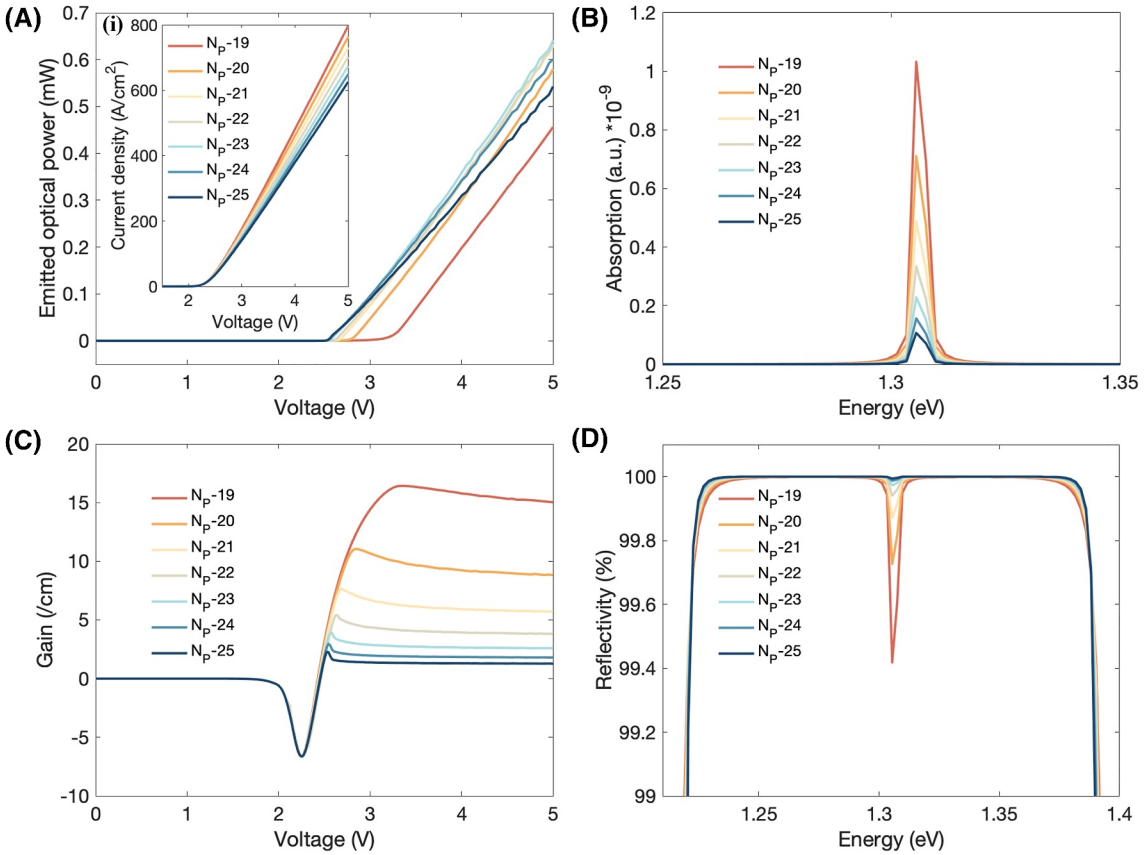

FIGURE 6 (A) The P-V curve with I-V curve as an inset, (B) the absorption spectrum of DBR, (C) the gain mode versus applied voltage of the EPVCSEL and (D) the reflectivity spectrum of DBR at different number of pairs (NP) of DBR. DBR, distributed Bragg reflector; EPVCSEL, electrically pumped vertical-cavity surface-emitting lasers.

reasonable as low absorption loss and high reflectivity enable device lasing much easier. Besides, the P_{out} increases and then decreases with the increase in N_P, reaching the optimized value when N_P is around 22. At low values of N_P, the loss is large, therefore, to achieve lasing, the gain needs to be larger to cover the loss as shown in Figure 6C which requires a large injection current. However, as the inset shows in Figure 6A, even when the current is at a maximum with N_P reaching 19, it still cannot compensate the loss, therefore, the P_{out} is the smallest. When N_P is larger than 23, although the loss is largely decreased, the gain mode is decreased to a level that is slightly larger than the loss to trigger stimulated recombination as we mentioned before. Therefore, the gain is largely decreased which leads to the decrease of P_{out}. Since the threshold voltages are comparable with each other when N_P is greater than 21, therefore, the optimized value for N_P is 22. Furthermore, we found that the resonant photon energy and the output longitudinal mode remained unchanged with the increase in N_P. The optimized thickness and doping concentration are listed in detail in the Table 3.

3.4 | The simulation of self-heating effect of the device

The heat generated in the MHP-EPVCSEL and the heat distribution inside the device are a significant research topic when the device is in operation. The lattice heat is governed by the following heat flow equation in SILVACO TCAD:

$$C_V \frac{\partial T_L}{\partial t} = \nabla(\kappa \nabla T_L) + H$$

where C_V, T_L, κ, and H are the heat capacitance per unit volume, the local lattice temperature, the thermal conductivity, and the heat generation, respectively. For halide perovskite materials, the κ is almost 2 orders lower than the InGaAsP/InP system. Therefore, knowing the thermal distribution of the devices during operation can determine their application circumstances. By using the optimal material and structure parameters obtained above, we can simulate the self-heating effect of the device in operation. Figure 7A is the 3D contour profile of the thermal distribution of the device in operation. It can be seen that the heat is mainly distributed in the active

TABLE 3 The optimized parameters of all the layers in the EPVCSEL.

Function layer	Material	Thickness (nm)	Doping concentration		Mobility		Layer number
			Acceptor ($/cm^3$)	Donor ($/cm^3$)	Electron ($cm^2V^{-1}s^{-1}$)	Hole ($cm^2V^{-1}s^{-1}$)	
Anode	ITO	100	-	$\sim10^{20}$	-	-	1
HIL	MoO_3	7	-	-	-	-	1
T-DBR	$CsSnCl_3$	108	5×10^{17}	-	5	5	22
	$MAPbCl_3$	130.5	5×10^{17}	-	5	5	22
OAEL1	$CsSnCl_3$	188	5×10^{17}	-	5	5	1
HTL	$CsSnCl_3$	130	5×10^{17}	-	5	5	1
AL	$CsSnI_3$	25	-	$\sim10^{17}$	5	5	1
ETL	$CsSnCl_3$	90	-	2×10^{17}	5	5	1
OAEL2	$CsSnCl_3$	208	-	5×10^{17}	5	5	1
B-DBR	$CsSnCl_3$	108	-	5×10^{17}	5	5	22
	$MAPbCl_3$	130.5	-	5×10^{17}	5	5	22
EIL	Cs	0.7	-	-	-	-	1
Cathode	Al	100	-	-	-	-	1

Abbreviations: EPVCSEL, electrically pumped vertical-cavity surface-emitting lasers.

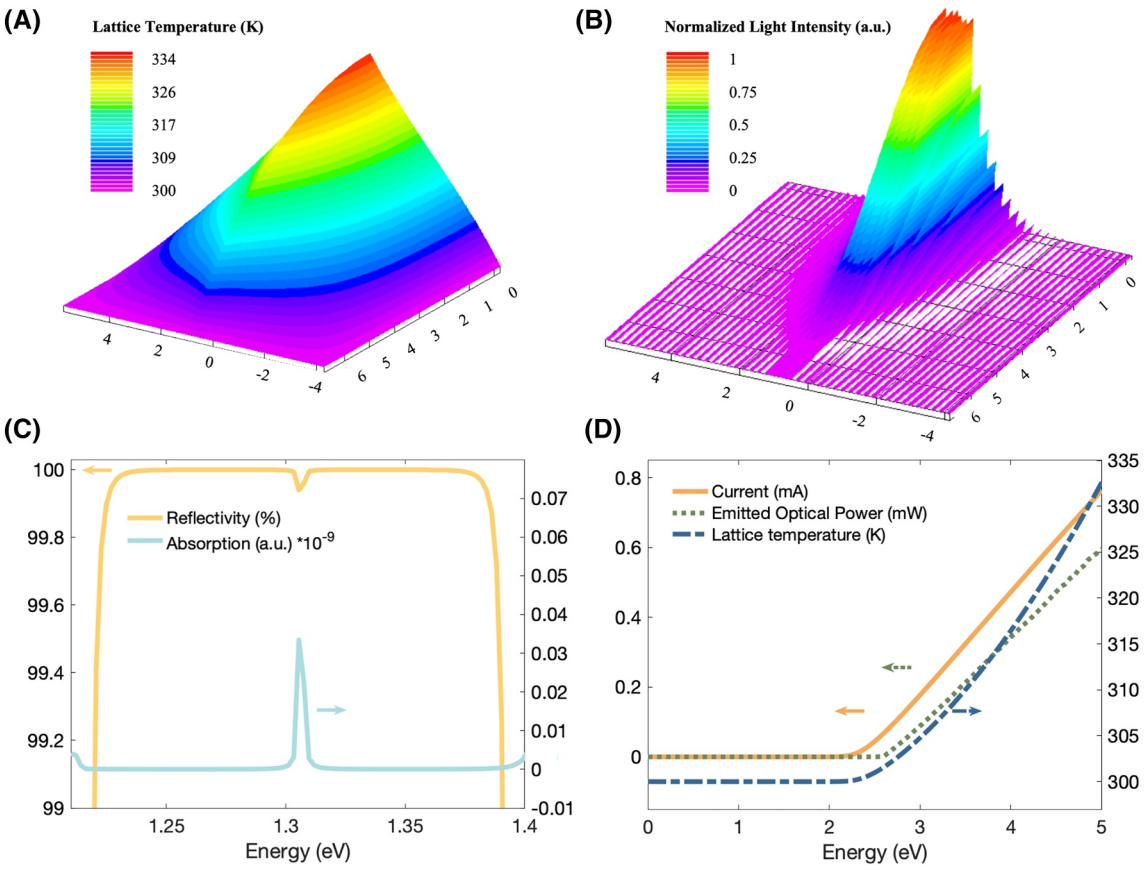

FIGURE 7 (A) The 3D thermal distribution image of the MHP-EPVCSEL device, (B) the profile of normalized light intensity, (C) the absorption and reflectivity spectrum of DBR, (D) the P-V curve, I-V curve, and the T_L-V curve of the device. DBR, distributed Bragg reflector; EPVCSEL, electrically pumped vertical-cavity surface-emitting lasers; MHP, metal halide perovskites.

region. The temperature is around 334 K when the applied voltage is 5 V, which is more than 30°C above room temperature. Figure 7B shows the beam shape of the emitted light which approaches a Gaussian distribution. Figure 7D shows that the T_L increases with the applied voltage, which implies that the device can realize the continuous wave at low driving voltage (3–4 V) with temperature ranging from 305 to 315 K, which is tolerable for halide perovskite.[42] However, if we want high output power, then thermal effect needs to be taken into consideration. The reflectivity, absorption, P-V curve, and I-V curve of the device are shown in Figure 7C,D), which serve as a reference for the self-heating simulation. For example, based on the I-V curve, we can obtain a threshold current density of about 69 A cm^{-2}, and from the P-V curve, we can obtain an output optical power of the order of 10^{-4} W.

4 | CONCLUSION

For the first time, we used halide perovskite materials to construct a high quality DBR optical resonant cavity and found out that when the NP of DBR is larger than 10, the reflectance can obtain more than 91%. Furthermore, we used the DBR to further design the MHP-EPVCSEL device and conduct numerical modeling of the device. Through device performance simulations and parameter optimizations, the optimal values of doping concentration, thickness, mobility, and NP of DBR are obtained. Additionally, using the optimal parameters, the self-heating effect of the device in operation is obtained and the result shows that our proposed device can realize light amplification when the driving voltage is 3 V and the corresponding lattice temperature is about 305 K, which has the potential to realize continuous wave lasing at room temperature. Moreover, the I-V and P-V characteristics show that the threshold current density and output optical can reach ~69 A cm^{-2} and ~10^{-4} W. Our work can provide good insight and device and materials design guidance for fabricating cost-effective MHP-EPVCSEL.

ACKNOWLEDGMENTS

Authors acknowledge the financial support from the EPSRC SWIMS (EP/V039717/1), Royal Society (RGS\R1 \221009 and IEC\NSFC\211201), Leverhulme Trust (RPG-2022-263) and Sêr Cymru program – Enhancing Competitiveness Equipment Awards 2022-23 (MA/VG/2715/22-PN66). Authors acknowledge Dongguk University for the Silvaco TCAD simulation support and constructive comments from Dr Chandra Kant.

CONFLICT OF INTEREST STATEMENT

The authors declare that there are no conflicts of interest related to this article.

DATA AVAILABILITY STATEMENT

Information on the data underpinning the results presented here, including how to access them, can be found in the Cardiff University data catalog at [https://doi.org/10.17035/cardiff.27117615].

ORCID

Bo Hou https://orcid.org/0000-0001-9918-8223

REFERENCES

1. Yoshikawa M, Murakami A, Sakurai J, Nakayama H, Nakamura T. In: *Proceedings Electronic Components and Technology*; 2005:1353-1358.
2. Naoto J, Akihiro I, Kazuhiro H, Toshihide S, Shunichi S. In: *Vertical-Cavity Surface-Emitting Lasers XX, SPIE*; 2016.976605.
3. Larsson A, Simpanen E, Gustavsson JS, et al. 1060 nm VCSELs for long-reach optical interconnects. *Opt Fiber Technol*. 2018; 44:36-42.
4. Yan D, Liu M, Li Z, Hou B. Colloidal quantum dots and metal halide perovskite hybridization for solar cell stability and performance enhancement. *J Mater Chem A*. 2021;9(28): 15522-15541.
5. Li B, Hou B, Amaratunga GAJ. Indoor photovoltaics, the Next Big Trend in solution-processed solar cells. *InfoMat*. 2021;3(5):445-459.
6. Zhan S, Fan X-B, Zhang J, et al. Lattice marginal reconstruction-enabled high ambient-tolerance perovskite quantum dot phototransistors. *J Mater Chem C*. 2020;8(45):16001-16009.
7. Worku M, Ben-Akacha A, Blessed Shonde T, Liu H, Ma B. The past, present, and future of metal halide perovskite light-emitting diodes. *Small Science*. 2021;1(8):2000072.
8. Im J-H, Kim H-S, Park N-G. Morphology-photovoltaic property correlation in perovskite solar cells: one-step versus two-step deposition of $CH_3NH_3PbI_3$. *Apl Mater*. 2014;2(8):081510.
9. Stoumpos CC, Malliakas CD, Kanatzidis MG. Semiconducting tin and lead iodide perovskites with organic cations: phase transitions, high mobilities, and near-infrared photoluminescent properties. *Inorg Chem*. 2013;52(15):9019-9038.
10. Liang Q, Liu K, Sun M, et al. Manipulating crystallization kinetics in high-performance blade-coated perovskite solar cells via cosolvent-assisted phase transition. *Adv Mater*. 2022; 34(16):2200276.
11. Zhang Z, Li Z, Chen Y, et al. Progress on inkjet printing technique for perovskite films and their optoelectronic and optical applications. *ACS Photonics*. 2023;10:3435-3450.
12. Park SM, Wei M, Lempesis N, et al. Low-loss contacts on textured substrates for inverted perovskite solar cells. *Nature*. 2023;624(7991):289-294.
13. Cui J, Liu Y, Deng Y, et al. Efficient light-emitting diodes based on oriented perovskite nanoplatelets. *Sci Adv*. 2021; 7(41):eabg8458.
14. Chiba T, Hayashi Y, Ebe H, et al. Anion-exchange red perovskite quantum dots with ammonium iodine salts for highly efficient light-emitting devices. *Nat Photonics*. 2018;12(11):681-687.

15. Zhao B, Bai S, Kim V, et al. High-efficiency perovskite–polymer bulk heterostructure light-emitting diodes. *Nat Photonics*. 2018;12:783-789.
16. Zhao F, Ren A, Li P, Li Y, Wu J, Wang ZM. Toward continuous-wave pumped metal halide perovskite lasers: strategies and challenges. *ACS Nano*. 2022;16(5):7116-7143.
17. Vincent P, Kim D-K, Kwon J-H, Bae J-H, Kim H. Correlating the nanoparticle size dependent refractive index of ZnO optical spacer layer and the efficiency of hybrid solar cell through optical modelling. *Thin Solid Films*. 2018;660:558-563.
18. Mei G, Wu D, Ding S, Choy WCH, Wang K, Sun XW. Optical tunneling to improve light extraction in quantum dot and perovskite light-emitting diodes. *IEEE Photon J*. 2020;12(6):1-14.
19. Ren Z, Sun J, Yu J, et al. High-performance blue quasi-2D perovskite light-emitting diodes via balanced carrier confinement and transfer. *Nano-Micro Lett*. 2022;14(1):66.
20. Liu R-J, Dong J-Y, Wang M-W, et al. Efficiency improvement of quantum dot light-emitting diodes via thermal damage suppression with HATCN. *ACS Appl Mater Interfaces*. 2021;13(41):49058-49065.
21. Dai X, Deng Y, Peng X, Jin Y. Quantum-Dot light-emitting diodes for large-area displays: towards the dawn of commercialization. *Adv Mater*. 2017;29(14):1607022.
22. Lee CW, Lee JY. A hole transport material with ortho-linked terphenyl core structure for high power efficiency in blue phosphorescent organic light-emitting diodes. *Org Electron*. 2014;15(2):399-404.
23. Tao S, Schmidt I, Brocks G, et al. Absolute energy level positions in tin- and lead-based halide perovskites. *Nat Commun*. 2019;10(1):2560.
24. Islam J, Hossain AKMA. Semiconducting to metallic transition with outstanding optoelectronic properties of CsSnCl3 perovskite under pressure. *Sci Rep*. 2020;10(1):14391.
25. He C, Zha G, Deng C, et al. Refractive index dispersion of organic–inorganic hybrid halide perovskite CH3NH3PbX3 (X═Cl, Br, I) single crystals. *Cryst Res Technol*. 2019;54(5):1900011.
26. Wang N, Zhou Y, Ju M-G, et al. Heterojunction-depleted lead-free perovskite solar cells with coarse-grained B-γ-$CsSnI_3$ thin films. *Adv Energy Mater*. 2016;6(24):1601130.
27. Srivastava S, Singh AK, Kumar P, Pradhan B. Comparative performance analysis of lead-free perovskites solar cells by numerical simulation. *J Appl Phys*. 2022;131(17):175001.
28. Frost JM. Calculating polaron mobility in halide perovskites. *Phys Rev B*. 2017;96(19):195202.
29. Maculan G, Sheikh AD, Abdelhady AL, et al. $CH_3NH_3PbCl_3$ single crystals: inverse temperature crystallization and visible-blind UV-photodetector. *J Phys Chem Lett*. 2015;6(19):3781-3786.
30. Matsushima T, Bencheikh F, Komino T, et al. High performance from extraordinarily thick organic light-emitting diodes. *Nature*. 2019;572(7770):502-506.
31. Lajaunie L, Boucher F, Dessapt R, Moreau P. Strong anisotropic influence of local-field effects on the dielectric response of α-MoO_3. *Phys Rev B*. 2013;88(11):115141.
32. Chung I, Song J-H, Im J, et al. $CsSnI_3$: semiconductor or metal? High electrical conductivity and strong near-infrared photoluminescence from a single material. High hole mobility and phase-transitions. *J Am Chem Soc*. 2012;134(20):8579-8587.
33. Haeger T, Heiderhoff R, Riedl T. Thermal properties of metal-halide perovskites. *J Mater Chem C*. 2020;8(41):14289-14311.
34. Atlas User's Manual Device Simulation Software. *Chapter 10 VCSEL Simulator*. SILVACO; 2015:567-583.
35. Lu J, Guan X, Li Y, et al. Dendritic $CsSnI_3$ for efficient and flexible near-infrared perovskite light-emitting diodes. *Adv Mater*. 2021;33(44):2104414.
36. Nunley TN, Fernando NS, Samarasingha N, et al. Optical constants of germanium and thermally grown germanium dioxide from 0.5 to 6.6eV via a multisample ellipsometry investigation. *J Vac Sci Technol B*. 2016;34(6):061205.
37. Filonov V, Filonova Y, Dubyk Y, Pis'mennyi E. Transfer matrix method for analysis of flow thermohydraulic characteristics with extremely nonlinear behavior of thermophysical properties using channel approach. *Int J Heat Mass Tran*. 2022;187:122531.
38. Chang J, Chen D, Yang L, et al. High-quality crystal growth and characteristics of AlGaN-based solar-blind distributed Bragg reflectors with a tri-layer period structure. *Sci Rep*. 2016;6(1):29571.
39. Fu H, Zhao Y. In: Huang JJ, Kuo H.-C, Shen S.-C, eds. *Nitride Semiconductor Light-Emitting Diodes (LEDs)*. 2nd ed. Woodhead Publishing; 2018:299-325.
40. Liu A, Guan G, Chai X, et al. Metal halide perovskites toward electrically pumped lasers. *Laser Photon Rev*. 2022;16(10):2200189.
41. Shaaban IE, Samra AS, Muhammad S, Wageh S. Design of distributed Bragg reflectors for green light-emitting devices based on quantum dots as emission layer. *Energies*. 2022;15(3):1237.
42. Afreen M, Ali J, Bilal M. Challenges of stability in perovskite solar cells. *Fundamentals of Solar Cell Design*. 2021:371-391.

SUPPORTING INFORMATION

Additional supporting information can be found online in the Supporting Information section at the end of this article.

How to cite this article: Liu R, Ji H, Othman DM, et al. Numerical simulation of electrically pumped active vertical-cavity surface-emitting lasers diodes based on metal halide perovskite. *InfoScience*. 2024;e12027. https://doi.org/10.1002/inc2.12027